## ARTICLE    OPEN

# The bulk-corner correspondence of time-reversal symmetric insulators

Sander Kooi[1], Guido van Miert[2] and Carmine Ortix [iD][1,2 ✉]

The topology of insulators is usually revealed through the presence of gapless boundary modes: this is the so-called bulk-boundary correspondence. However, the many-body wavefunction of a crystalline insulator is endowed with additional topological properties that do not yield surface spectral features, but manifest themselves as (fractional) quantized electronic charges localized at the crystal boundaries. Here, we formulate such bulk-corner correspondence for the physical relevant case of materials with time-reversal symmetry and spin-orbit coupling. To do so we develop partial real-space invariants that can be neither expressed in terms of Berry phases nor using symmetry-based indicators. These previously unknown crystalline invariants govern the (fractional) quantized corner charges both of isolated material structures and of heterostructures without gapless interface modes. We also show that the partial real-space invariants are able to detect all time-reversal symmetric topological phases of the recently discovered fragile type.

## INTRODUCTION

The discovery of topological insulators has fundamentally challenged our common classification of materials in terms of electrical insulators and electrical conductors[1,2]. Topological insulators are in fact materials that are insulating in their bulk but allow for perfect conduction of electrical currents along their surfaces. This macroscopic physical property is the immediate consequence of the topological properties of the ground state of the insulator: this is the essence of the so-called bulk-boundary correspondence. In a topological insulator, the electrical conduction is protected against different detrimental effects since the surface electronic modes have an anomalous nature. The chiral states appearing at the edge of a quantum Hall insulator, for instance, represent anomalous states since in a conventional one-dimensional atomic chain it is impossible to find a different number of left-moving and right-moving electrons[3,4]. The helical edge states of quantum spin-Hall insulators[5–9], as well as the single Dirac surface states of strong three-dimensional topological insulators[10–15] violating the fermion doubling theorem, are other prime examples of such anomalies.

When unitary spatial symmetries are taken into account, additional topological crystalline phases can arise[16–20]. The non-trivial topology of the system then guarantees the presence of anomalous surface states appearing only on surfaces that are left invariant under the protecting crystalline symmetry, and which violate stronger versions of the fermion doubling theorem[21]. Furthermore, crystalline symmetries can lead to a class of insulating phases, dubbed higher-order topological insulators, with conventionally gapped surface states but with anomalous gapless states appearing on the hinges connecting two surfaces related to each other by the crystalline protecting symmetry[22–27].

The single Slater determinant describing the ground state of a non-interacting crystalline insulator generally possesses additional topological indices that are not immediately related to the presence or absence of anomalous gapless surface states. For instance, the electric polarization of an inversion-symmetric one-dimensional atomic chain is either integer or semi-integer, with a quantized value that does not depend upon microscopic details, but is rather encoded in a gauge-invariant topological index[28]. More recently, it has been shown that excess electronic charges localized at various topological defects, such as dislocations, can be (fractionally) quantized, thus representing yet other incarnations of bulk quantities encoded in topological invariants[29–34]. Quantized charges appearing at the corners and disclinations of two-dimensional crystals have been very recently measured in metamaterials[35–37] and proposed to appear in recently synthesized materials structures[38]. Together with the topological indices dictating the presence of anomalous gapless surface modes, the gauge-invariant bulk quantities governing the appearance of quantized defect charges specify the entire observable topological content of a crystal.

In systems with broken time-reversal symmetry this set of crystalline topological invariants can be entirely expressed in terms of the symmetry properties of the occupied single particle Bloch states at the high-symmetry points of the Brillouin zone with the addition of the Chern number. However, for the physically relevant case of materials with spin–orbit coupling and time-reversal symmetry eigenvalues-based schemes do suffer of intrinsic limitations. Topological crystalline phases with robust boundary modes may pass completely undetected[39] using the current classification schemes based on symmetry indicators[40–44]. Likewise, the real-space invariants originally introduced in ref. [24] are insufficient to determine the quantized excess charges. This is because Kramers' theorem inevitably doubles the electronic charges, making the real-space invariants partially, often completely, trivial. Progress can be made identifying (partial) Berry phase[29] invariants and/or using Wilson loops as topological indices[45–49] as exemplified by the bulk-dislocation charge correspondence of rotation-symmetric two-dimensional crystals[31]. This additional knowledge, however, does not completely determine the (fractional) quantized electronic charges at the crystal boundaries.

[1]Institute for Theoretical Physics, Center for Extreme Matter and Emergent Phenomena, Utrecht University, Princetonplein 5, 3584 CC Utrecht, the Netherlands. [2]Dipartimento di Fisica E. R. Caianiello, Università di Salerno, I-84084 Fisciano Salerno, Italy. ✉email: c.ortix@uu.nl
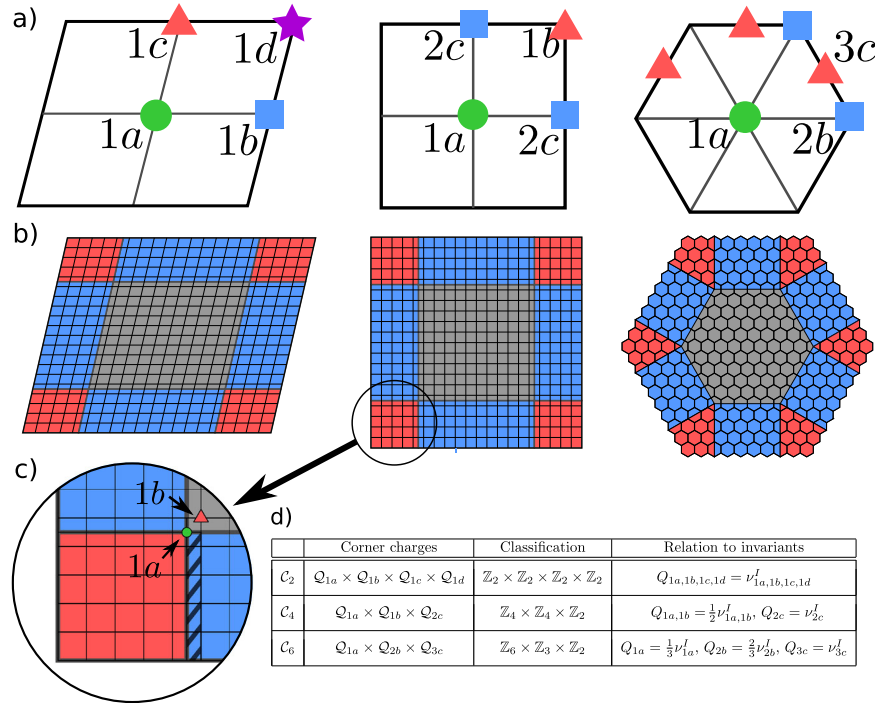
**Fig. 1 Bulk and corners of two-dimensional rotation-symmetric crystals. a** Unit cells of rotation-symmetric crystals. The special Wyckoff positions and their multiplicities are explicitly indicated. **b** Rotation-symmetric crystals in open-disk geometries. The red, blue, and gray regions indicates bulk, edges, and corners, respectively. Note that when considering a reference $\mathcal{C}_2$-symmetric Wyckoff position, the corner charge has to be summed over the adjacent corners not related by $\mathcal{C}_2$ symmetry in order to represent a quantized bulk quantity. **c** Zoom in of the $\mathcal{C}_4$-symmetric corners with the two possible reference Wyckoff positions. **d** Table of the corner charge topological characterization for $\mathcal{C}_2, \mathcal{C}_4$, and $\mathcal{C}_6$ symmetric systems.

Here, we overcome these hurdles by developing a strategy that for two-dimensional time-reversal symmetric insulators in rotation symmetric crystals is able to fully resolve this missing bulk-corner correspondence. The crux of our analysis is the ability to effectively deduplicate the real-space invariants of ref. [24], using a computationally efficient framework that requires only the knowledge of the Bloch wavefunctions throughout the Brillouin zone. We show that the resulting partial real-space invariants govern not only the quantized corner charges of insulators that are deformable to atomic limit, but also determine the quantized corner charges in heterostructures comprising topologically distinct quantum spin-Hall insulators. Even more importantly, the bulk-corner correspondence we formulate here allows the detection of all topological states of the fragile type[50,51] in time-reversal symmetric crystals, in much the same way as the recently introduced twisted bulk-boundary correspondence is able to diagnose fragile phases in systems without spin–orbit coupling[52,53].

Before presenting our results, let us discuss in more detail the intrinsic limitations of symmetry-based eigenvalue schemes in detecting the (fractionally) quantized corner charges characterizing all time-reversal symmetric insulators that do not feature metallic edge modes. Let us consider for simplicity a crystal with a simple twofold rotation symmetry $\mathcal{C}_2$. At the high-symmetry points in the Brillouin zone (BZ) $\Gamma = (0, 0)$, $X = (\pi, 0)$, $Y = (0, \pi)$, and $M = (\pi, \pi)$, the $\mathcal{C}_2$ symmetry provides us with eight natural numbers $\Gamma_{\pm i}, \ldots, M_{\pm i}$, which denote the multiplicities of occupied Bloch states with rotation eigenvalues $\pm i$ (from here onwards we will consider systems of spin 1/2 fermions). These multiplicities, taken by themselves, define proper integer invariants since they can only change by bandgap closing and reopening processes. However, the multiplicities at different momenta are not linearly independent because of the presence of the compatibility relations $HS_i + HS_{-i} = N_F$ with $HS = \Gamma, X, Y, M$ and $N_F$ the number of occupied bands. Even more importantly, the rotation symmetry multiplicities do not correspond to any known physical observable.

These shortcomings can, however, be overcome by constructing the linear combinations of the multiplicities originally introduced in ref. [24], recently dubbed real-space invariants[52]. For a $\mathcal{C}_2$-symmetric insulator this approach gives rise to four $\mathbb{Z}$-numbers $v_{1a}, \ldots, v_{1d}$ in one-to-one correspondence with the four $\mathcal{C}_2$-symmetric Wyckoff positions $1a, \ldots, 1d$ [Fig. 1]. As a result, we find a global $\mathbb{Z}^4$ classification, which is fully in agreement with $K$-theory studies[54]. Moreover, the parities of these real-space invariants dictate the values of the fractional part of the quantized charge contained in corners measured with respect to $\mathcal{C}_2$-symmetric Wyckoff positions [Fig. 1]. For example, if $v_{1a}$ is an even (odd) integer then the corner charge $Q_{1a}$ measured with respect Wyckoff position $1a$ is equal to 0 (1/2) mod 1, i.e., $Q_{1a} = v_{1a}/2 \bmod 1$. Note that only the fractional part of the corner charge represents a proper bulk value, as the possible occurrence of in-gap corner modes affects the integer part. In other words, we cannot distinguish between $Q_{1a} = 0$ and $Q_{1a} = 1$ from a topological point of view.

The above one-to-one correspondence between symmetry labels (encoded in $v_{1x}$'s) and the fractional part of the quantized corner charges is completely general and applies to all rotation-symmetric two-dimensional crystals. Specifically, the corner charges measured with respect to a special Wyckoff position with a site symmetry group containing an $n$-fold rotation symmetry has a fractional part quantized in multiples of $1/n$, thereby defining a $\mathbb{Z}_n$ topological invariant. Beside the $\mathbb{Z}_2^2$ classification of $\mathcal{C}_2$-symmetric crystals discussed above, this leads to $\mathbb{Z}_4 \times \mathbb{Z}_4 \times \mathbb{Z}_2$ classification in fourfold rotation symmetric crystals and a $\mathbb{Z}_6 \times \mathbb{Z}_3 \times \mathbb{Z}_2$ classification [Fig. 1a, d] with the invariants all formulated in terms of symmetry labels [Supplementary Note I].

Even though the discussion above is informative from a purely theoretical point of view and of relevance to metamaterial structures, it has a limited value for the large number of insulating materials which possess time-reversal symmetry. This is because Kramers' theorem dictates that the corner charges measured with respect to a $\mathcal{C}_n$-symmetric Wyckoff position must be quantized in multiples of $2/n$[30,46]. This clearly trivializes the $\mathbb{Z}_2^4$ topological content of twofold rotation symmetric crystals, whereas it leaves two residual $\mathbb{Z}_2$ topological invariants – corresponding to the (semi)integer values of the corner charges relative to the Wyckoff positions $1a$ and $1b$ [see Fig. 1] – in fourfold rotation symmetric crystals and a $\mathbb{Z}_3 \times \mathbb{Z}_3$ classification in $\mathcal{C}_6$-symmetric crystals. The doubling does not alter the classification of $\mathcal{C}_3$-symmetric corners, thus implying that in threefold rotation-symmetric crystals real-space invariants can be redefined even in time-reversal symmetric conditions.

For evenfold rotation-symmetric corners, and this is key, the trivialization of the corner charges is instead only apparent. Kramers' theorem not only engenders the doubling of the corner charge quantum from $1/n$ to $2/n$; it further guarantees that microscopic details at the edge and corners of a finite size crystal can only change the value of the corner charge by an even integer rather than an integer. This can be immediately seen from the fact that when created by local perturbations in-gap corner modes have to come in pairs. In other words, now the cases $Q_{1a} = 0$ and $Q_{1a} = 1$ are topologically distinct.

The fact that in time-reversal symmetric conditions the corner charges *modulo* 2 are bulk quantities has a twofold effect. First, it implies that from a corner-charge perspective the topological crystalline characterization of rotation-symmetric insulators is the one tabled in Fig. 1d even in the presence of time-reversal symmetry. Second, and most importantly, the quantized corner charges cannot be simply expressed in terms of the symmetry eigenvalues: consider the simple case of a $\mathcal{C}_2$-symmetric insulator. Time-reversal symmetry requires that all the integers $\Gamma_{\pm i} \ldots M_{\pm i} \equiv N_F/2$ rendering the real-space invariants [Supplementary Note I and ref. 24] completely trivial. Furthermore, the quantized (partial) Berry phases[29] on the high-symmetry $k_{x,y} \equiv 0$ lines of the BZ only provide a $\mathbb{Z}_2^2$ classification that, as such, is not able to resolve the quantized corner charges. A different approach would be to explicitly construct Wannier functions respecting the crystalline symmetries and subsequently compute the gauge-invariant Wannier centers[55]. This requires however the use of a projection procedure[56] that can yield singularities if the chosen set of trial atomic orbitals does not possess the symmetry properties of the targeted symmetric Wannier functions. Additionally, the explicit construction of symmetric Wannier functions is by definition not applicable to fragile topological insulators which still possess quantized corner charges.

## RESULTS

### Partial real-space invariants

Having established that in time-reversal symmetric conditions the quantized values of the corner charges cannot be entirely read off from the point-group symmetries eigenvalues or from Berry phase indicators, we next derive the bulk-corner correspondence by formulating crystalline topological invariants entirely different in nature. Our approach can be decomposed into three steps: we start from a particularly stringent set of assumptions that will be partially relaxed in each consecutive step by employing the $\mathcal{U}(N_F)$ gauge degree of freedom of the many-body wavefunction. The end product of this endeavor will be a formulation of crystalline invariants that can readily be computed using standard numerical methods.

Let us first notice that as long as we consider insulators whose ground state can be described in terms of exponentially localized Wannier functions, and thus adiabatically connected to an atomic insulator, the formulation of the topological invariants governing the quantized corner charges with time-reversal symmetry only requires a bulk expression for the number of Wannier Kramers' pairs centered at the special Wyckoff positions in the unit cell. Such a formulation can be immediately achieved by considering a simple subclass of time-reversal invariant insulators, i.e., systems without sizable spin–orbit coupling. In this materials class, we can naturally split the space of occupied Bloch states into two sectors related to each other by time-reversal symmetry: sector $I$ for spin-up electrons, and sector $II$ for the spin-down electrons. Importantly, choosing the spin quantization axis perpendicular to the crystalline plane each sector enjoys the $\mathcal{C}_n$ rotation symmetry of the lattice. This also implies that the fractional part of the corner charge in each sector can be related to the real-space invariants introduced in ref. 24 via $Q_{Nx}^{I,II} = m v_{mx}^{I,II}/n$ where $m$ indicates the multiplicity of the Wyckoff position $mx$ with respect to which the corner charge is measured. Moreover, time-reversal symmetry guarantees that the corner charges associated to two channels are equal, i.e., $Q_{1x}^I = Q_{1x}^{II}$. As a result, the quantized corner charge of time-reversal symmetric insulators are given by

$$Q_{mx} = 2 Q_{mx}^I = \frac{2 m v_{mx}^I}{n} \mod 2. \tag{1}$$

We naturally dub these integers partial real-space invariants in analogy with the partial Berry phase. Although the partial real-space invariants have been derived in the context of Wannier-azible insulators, they apply equally well to topological states of the fragile type. These recently discovered topological states cannot be represented in terms of symmetric Wannier functions[50,51], but at the same time they do not feature gapless edge states. Being insulating both in their bulk and along their edges, they are characterized by quantized corner charges at $\mathcal{C}_n$-symmetric corners. Furthermore, the hallmark of fragile phases is their decay into an atomic insulating phase by a proper addition of topologically trivial bands. The additivity of the corner charges under band additions then engenders the validity of the partial real-space invariants.

The absence of spin–orbit coupling considered so far provides us with a natural splitting of the Bloch states in two sectors related to each other by time-reversal symmetry and separately $\mathcal{C}_n$-symmetric. However, taking advantage of the $\mathcal{U}(N_F)$ gauge degree of freedom that leaves the Slater determinant unchanged, such a decomposition can be always achieved, even in systems with a sizable spin–orbit coupling. The problem of determining the corner charge therefore boils down to finding a continuous, periodic, and rotation-symmetric gauge for two time-reversed sectors, and subsequently computing the real-space invariants for a single sector. There is, however, a small caveat. Namely, in our derivation we have implicitly been assuming that the Chern number per sector vanishes. This follows from the fact that the real-space invariants from ref. 24 only apply to systems without chiral edge states. Hence, by relying on precisely those invariants we have to demand that the Chern numbers of each sector vanish, i.e., $C^I \equiv C^{II} \equiv 0$. Note that this represents an additional constraint on the gauge as time reversal symmetry only guarantees that $C^I + C^{II} \equiv 0$.

Our second step consists in relaxing precisely this additional constraint on the sector Chern numbers $C^{I,II}$. To do so, we will invoke the gauge invariance principle. More specifically, we will modify the invariants such that their values are invariant under residual gauge transformations, i.e., those transformations that preserve the rotational and time-reversal symmetry constraints. We can distinguish between two different flavors of residual gauge transformations: small and large. Small residual gauge transformations are defined as those gauge transformations that can be smoothly deformed to the identity whilst preserving the symmetry constraints. In particular, these small gauge

transformations include gauge transformations that do not rotate the two time-reversed sectors into each other. The invariance under small gauge transformations does not pose additional constraints on the partial real space invariants defined before: the $v^l_{mx}$'s are already immune to these gauge transformations. However, using that the sector Chern number $C^l$ is also invariant under small residual gauge transformations we are entitled to extend the definition of the invariants $v^l_{mx}$ to sectors with non-zero Chern numbers. Indeed, this may be achieved with the following linear combination:

$$v^l_{mx} \rightarrow v^l_{mx} + \alpha C^l, \tag{2}$$

with $\alpha$ constant whose value will be fixed upon requiring the invariance under large gauge transformations. Before doing so, let us remark that the right-hand side of the equation above is the simplest expression that reduces to the original $v^l_{mx}$'s for vanishing sector Chern number while being still additive. Next, we impose the invariance under large gauge transformations to fix the value of $\alpha$. By definition large transformations are not deformable to the identity (or at least not without breaking the symmetries in between). Let us assume, similarly to ref. [7], that in the energy spectrum there are no degeneracies other than those required by time-reversal symmetry. In this case there is only one large gauge transformation: it amounts to exchanging the time-reversed channel labels $I \leftrightarrow II$ in a $n$-th, pair of bands. It is straightforward to see that the sector Chern number transforms according to $C^l \rightarrow C^l - 2C^l_n$ where $C^l_n$ is the sector Chern number of the $n$-th pair. The large gauge transformation clearly transforms also the sector symmetry eigenvalues. Let us explicitly consider the case of a twofold rotation symmetric crystal for which the zero Chern numbers partial real space invariant

$$v^l_{1a} = \Gamma^l_i + \frac{1}{2}[\Gamma^l_{-i} - X^l_{-i} - Y^l_{-i} - M^l_{-i}]. \tag{3}$$

Under the time-reversed channels exchange in the $n$-th pair of band, each of the $\mathcal{C}_2$ eigenvalue multiplicities at the high symmetry points of the BZ is modified according to $HS_{\pm i} \rightarrow HS_{\pm i} \pm i \, \zeta^l_n(HS)$ where $\zeta^l_n$ is the twofold rotation symmetry eigenvalue at $HS = \Gamma, X, Y, M$. This consequently implies that $v^l_{1a} \rightarrow v^l_{1a} + i\sum_{HS}\zeta^l_n(HS)/2 = v^l_{1a} + C^l_n \bmod 2$ where in the last equality we used the relation between the parity of the Chern number and the $\mathcal{C}_2$ eigenvalues[57]. The knowledge of these transformation properties enables us to define a modified partial real space topological integer that remain invariant under large gauge transformation by taking $\alpha = 1/2$. Hence, the final expression for the invariant $v^l_{1a}$ reads

$$v^l_{1a} = \frac{1}{2}C^l + \Gamma^l_i + \frac{1}{2}[\Gamma^l_{-i} - X^l_{-i} - Y^l_{-i} - M^l_{-i}]. \tag{4}$$

Next, we explicitly verify the gauge invariance of the integer in the equation above by discussing a paradigmatic microscopic model. Consider a bilayer system consisting of two Kane–Mele models[5] on a uniaxially strained honeycomb lattice, with the two models differing only by the relative sign of the intrinsic spin–orbit coupling strength $\lambda_{ISO}$. Being the sum of two quantum spin-Hall insulators, the bilayer system does not possess metallic edge states, and therefore the bulk corner correspondence is well posed. We first determine the partial real-space invariants by decomposing the space of occupied Bloch states according to their spin $s_z$ eigenvalues. Having chosen the sign of $\lambda_{ISO}$ opposite in the two layers, each of the spin state has a vanishing Chern number. Therefore, we can safely use the formulation of the invariants in terms of the individual channel symmetry eigenvalues. It can be easily shown that the non-zero multiplicities of the residual $\mathcal{C}_2$ rotation symmetry are $\Gamma^l_i = X^l_i = Y^l_i = M^l_{-i} = 2$. Consequently, the partial real-space invariant of Eq. (4)$v^l_{1a} = 1$ immediately predicts a quantized corner charge measured with respect to the center of the unit cell $Q_{1a} = v^l_{1a} \bmod 2 = 1 \bmod 2$. Next, we

**Table 1.** Partial real-space invariants of rotation-symmetric two-dimensional insulators.

| | |
|---|---|
| $\mathcal{C}_2$ | $v^l_{1a} = \frac{1}{2}C^l + \Gamma^l_i + \frac{1}{2}\left[\Gamma^l_{-i} - X^l_{-i} - Y^l_{-i} - M^l_{-i}\right]$ |
| | $v^l_{1b} = \frac{1}{2}C^l - \frac{1}{2}\left[\Gamma^l_{-i} - X^l_{-i} + Y^l_{-i} - M^l_{-i}\right]$ |
| | $v^l_{1c} = \frac{1}{2}C^l - \frac{1}{2}\left[\Gamma^l_{-i} + X^l_{-i} - Y^l_{-i} - M^l_{-i}\right]$ |
| | $v^l_{1d} = \frac{1}{2}C^l - \frac{1}{2}\left[\Gamma^l_{-i} - X^l_{-i} - Y^l_{-i} + M^l_{-i}\right]$ |
| $\mathcal{C}_4$ | $v^l_{1a} = -\frac{1}{2}C^l + \left(-3\Gamma^l_{e^{i\pi/4}} - \frac{3}{2}\Gamma^l_{e^{i3\pi/4}} - \Gamma^l_{e^{-i3\pi/4}} - \frac{3}{2}\right.$ |
| | $\left. \times \, \Gamma^l_{e^{-i\pi/4}} + \frac{3}{2}M^l_{e^{i3\pi/4}} + 2M^l_{e^{-i3\pi/4}} + \frac{3}{2}M^l_{e^{-i\pi/4}} + X^l_{-i}\right)$ |
| | $v^l_{1b} = -\frac{1}{2}C^l + \left(\frac{3}{2}\Gamma^l_{e^{i3\pi/4}} + 2\Gamma^l_{e^{-i3\pi/4}} + \frac{3}{2}\Gamma^l_{e^{-i\pi/4}}\right.$ |
| | $\left. -\frac{1}{2}M^l_{e^{i3\pi/4}} - 2M^l_{e^{-i3\pi/4}} - \frac{1}{2}M^l_{e^{-i\pi/4}} - X^l_{-i}\right)$ |
| | $v^l_{2c} = \frac{1}{2}C^l + \frac{1}{2}\left(\Gamma^l_{e^{i3\pi/4}} + \Gamma^l_{e^{-i\pi/4}} - M^l_{e^{i3\pi/4}} - M^l_{e^{-i\pi/4}}\right)$ |
| $\mathcal{C}_6$ | $v^l_{1a} = -\frac{1}{2}C^l + \left(-5\Gamma^l_{e^{i\pi/6}} - \frac{5}{2}\Gamma^l_{e^{i\pi/2}} - \Gamma^l_{e^{i5\pi/6}} - \frac{1}{2}\Gamma^l_{e^{-i5\pi/6}}\right.$ |
| | $\left. -\Gamma^l_{e^{-i\pi/2}} - \frac{5}{2}\Gamma^l_{e^{-i\pi/6}} + \frac{3}{2}M^l_{-i} + 2K^l_{-1} + 2K^l_{e^{-i\pi/3}}\right),$ |
| | $v^l_{2b} = C^l + \left(\Gamma^l_{e^{i\pi/2}} + \Gamma^l_{e^{i5\pi/6}} + \Gamma^l_{e^{-i\pi/2}} + \Gamma^l_{e^{-i\pi/6}}\right.$ |
| | $\left. -K^l_{-1} - K^l_{e^{-i\pi/3}}\right),$ |
| | $v^l_{3c} = \frac{1}{2}C^l + \frac{1}{2}\left(\Gamma^l_{e^{i\pi/2}} + \Gamma^l_{e^{-i5\pi/6}} + \Gamma^l_{e^{-i\pi/6}} - M^l_{-i}\right).$ |

employ a different decomposition wherein a channel is composed by a spin state, say spin up, in the first layer and the opposite spin state, spin down, in the second layer. This leads to different $\mathcal{C}_2$ multiplicities $\Gamma_{\pm i} = X_{\pm i} = Y_{\pm i} = M_{\pm i} = 1$ accompanied, however, by a non-vanishing Chern number in the two sectors $C^{I,II} = \pm 2$. The $\mathcal{C}_2$-protected topological index, modulo 2, is independent of the specific channel decomposition: Eq. (4) still verfies $v^l_{1a} \bmod 2 \equiv 1$. This is sufficient to resolve the quantized bulk corner charges of a twofold rotation symmetric insulator in time-reversal conditions while relaxing the constraint on the section Chern numbers. Note that these redefined partial real-space invariants [Table 1 and Supplementary Note II for their expressions also in the $\mathcal{C}_{4,6}$ cases] cannot be applied, per se, in systems with an odd channel Chern number. These systems realize quantum spin-Hall insulators and, in isolation, do not have a well-defined bulk-corner correspondence because of their gapless edges.

Having at hand explicit expressions without constraints on the channel Chern number immediately implies that the partial real-space invariants can be computed if we are provided with a continuous and periodic set of projectors $\rho^{I,II}(q) = \sum_m |\Psi^{I,II}_m(\vec{q})\rangle\langle\Psi^{I,II}_m(\vec{q})|$, related to each other by time-reversal symmetry and individually rotation symmetric. This is different from the former construction of a set of smooth, periodic, and symmetric Bloch waves $|\Psi^{I,II}_m(q)\rangle$ throughout the entire Brillouin zone, which necessitates individual Wannierazable channels. More importantly, we can now employ our third step and relax the constraint on the continuity, periodicity, and symmetry requirements on $\rho^{I,II}(q)$. As before, let us consider for simplicity $\mathcal{C}_2$ crystals and assume to have hypothetically found a set of continuous, periodic, and rotation symmetric projectors $\rho^{I,II}(q)$. First, we observe that this is precisely equivalent to having a continuous, smooth and periodic set of Bloch waves $|\Psi^{I,II}_m(\vec{q})\rangle$ in the effective Brillouin zone $EBZ = [0, \pi] \times [-\pi, \pi]$ (see Fig. 2) such that

(i) the sewing matrix $S_{\mathcal{C}_2}(\vec{q}) = \langle\Psi^\alpha_m(-\vec{q})|\mathcal{C}_2|\Psi^\beta_m(\vec{q})\rangle$ is block-diagonal along the two rotation symmetric high-symmetry lines $q_x = 0, \pi$;

(ii) the sewing matrix $S_{\mathcal{C}_2\Theta}(\vec{q}) = \langle\Psi^\alpha_m(\vec{q})|\mathcal{C}_2\Theta|\Psi^\beta_n(\vec{q})\rangle$ is block off-diagonal in the entire EBZ. In particular the Bloch waves in each channel can be redefined to satisfy $|\Psi^{II}_m(\vec{q})\rangle = \mathcal{C}_2\Theta|\Psi^I_m(\vec{q})\rangle$, in which case the sewing matrix $S_{\mathcal{C}_2\Theta}(\vec{q})^{\alpha,\beta}_{m,n} = \sigma^{\alpha,\beta}_x \delta_{m,n}$ with $\sigma_x$ the first Pauli matrix and $\delta_{m,n}$ the Kronecker delta.

We next use that since the Bloch waves along the boundary $\partial EBZ$ of the EBZ are smooth, periodic, and satisfy the symmetry
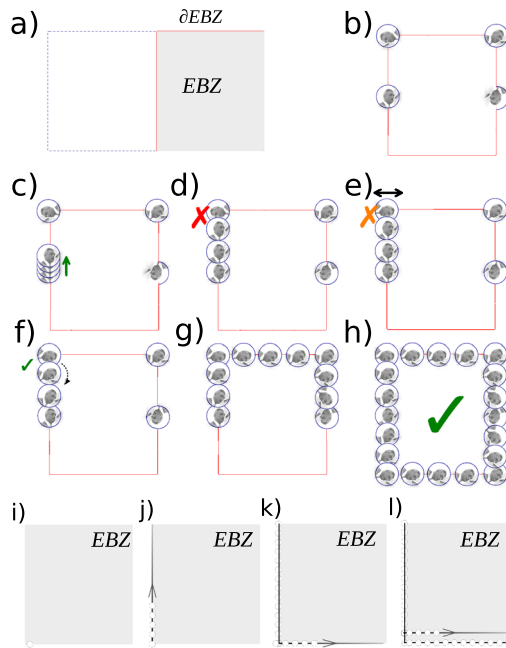
**Fig. 2 Schematic overview of the procedure to construct a $\mathcal{C}_2$ and $\Theta$-symmetric gauge along the effective Brillouin zone.** The gauge at each point is represented by a portrait of Felix Bloch. The $\mathcal{C}_2\Theta$-respecting gauge transformations are rotations of Bloch's portrait, possibly followed by a reflection. **a**) Brillouin zone, with in gray the effective Brillouin zone. **b**) Selection of $\mathcal{C}_2$- and $\Theta$-symmetric target Bloch states at the four high-symmetry points within EBZ. **c**) A continuous gauge is obtained along the line connecting $\Gamma$ and $Y$ by parallel transporting the target state at $\Gamma$ in the direction of $Y$. **d**) Topological mismatch between the parallel-transported states at $Y$ and the target Bloch states at $Y$. **e**) The topological mismatch at $Y$ reduces to a trivial mismatch upon redefining the target states at $Y$. The redefinition is represented as a mirror operation on the portrait of Bloch. **f**) The trivial mismatch is removed by a rotation that is evenly spread out over the parallel-transported states along the line connecting $Y$ and $\Gamma$. **g**) Pictorial representation of continuous $\mathcal{C}_2$ and $\Theta$-symmetric gauge along the upper half of the effective Brillouin zone boundary. **h**) Extension of the continuous $\mathcal{C}_2$- and $\Theta$-symmetric gauge along the entire effective Brillouin zone boundary. **i–l**) Procedure to construct a $\mathcal{C}_2$- and $\Theta$-symmetric gauge in the interior of the EBZ by parallel transport.

constraints, the Chern number contribution to the partial real-space invariants can be rewritten using Stokes' theorem as the contour integral of the Berry connection

$$\frac{1}{2}C^I \equiv \frac{1}{2\pi}\oint_{\partial EBZ} d\vec{q}\cdot Tr(\vec{A}^I(\vec{q})), \tag{5}$$

where we emphasize that the equation above is a true equality, and does not have any integer ambiguity. Considering that the multiplicities of the rotation symmetry eigenvalues are also uniquely determined by the Bloch waves along $\partial EBZ$, one could conclude that the computation of the partial real-space invariants, e.g., Eq. (4), can be reduced to an effective one-dimensional problem.

However, Eq. (5) constitutes a true equality only if the Bloch waves in both time-reversed channels are continuous, periodic, and symmetric throughout the entire effective Brillouin zone. If we were to abandon this constraint, then the halved Chern number $C^I/2$ would be only determined modulo an integer that is insufficient to determine, modulo 2, the partial real-space invariants. To make further progress, let us consider the effect upon the smooth Bloch waves in the entire EBZ of a $\mathcal{U}(N_F)$ transformation that preserves the block off-diagonal form of the $\mathcal{C}_2\Theta$ sewing matrix. We will refer to this subset of unitary

transformations as $\mathcal{U}_{\mathcal{C}_2\Theta}(N_F)$. It can be shown that this group of transformations constitutes a subgroup conjugate to the orthogonal group $\mathcal{O}(N_F)$ [see Supplementary Note III]. As a result, we have that the homotopy classes of $\mathcal{U}_{\mathcal{C}_2\Theta}(N_F)$ are the same as those of the orthogonal group. Specifically, $\mathcal{U}(N_F)_{\mathcal{C}_2\Theta}$ consists of two connected components:

$$\pi_0(\mathcal{U}(N_F)_{\mathcal{C}_2\Theta}) = \mathbb{Z}_2, \tag{6}$$

corresponding to the subset of matrices with determinant equal to $+1$ and $-1$. Moreover, as the first homotopy group of the orthogonal group is non-trivial, we find that the same applies to $\mathcal{U}(N_F)_{\mathcal{C}_2\Theta}$. In particular, this yields:

$$\pi_1(\mathcal{U}(N_F)_{\mathcal{C}_2\Theta}) = \begin{cases} \mathbb{Z} & \text{if } N_F = 2, \\ \mathbb{Z}_2 & \text{if } N_F > 2. \end{cases} \tag{7}$$

In other words, a map from a closed loop to our group of unitary transformations is either characterized by a $\mathbb{Z}$- or by a $\mathbb{Z}_2$-winding number. Since the effective Brillouin zone boundary, $\partial EBZ$, defines a closed loop, we can introduce the $\mathbb{Z}_2$-type winding number $W(\mathcal{U}|_{\partial EBZ})$. This $\mathbb{Z}_2$ winding number is of utmost importance since it allows us to uniquely determine how the halved sector Chern number, modulo 2, transforms under a $\mathcal{U}_{\mathcal{C}_2\Theta}$ transformation. We can therefore introduce other partial real-space invariants that are identical, modulo 2, to the expressions of Table 1 and thus correctly capture the bulk-corner correspondence. For instance, the analog of Eq. (4) can be written as

$$\begin{aligned} v^I_{1a} = {} & \frac{1}{2\pi}\oint_{\partial EBZ} d\vec{q}\cdot Tr(\vec{A}^I(\vec{q})) + W(U|_{\partial EBZ}) \\ & + \Gamma^I_i + \frac{1}{2}[\Gamma^I_{-i} - X^I_{-i} - Y^I_{-i} - M^I_{-i}] \end{aligned} \tag{8}$$

Since the expression above is invariant under arbitrary gauge transformations along the boundary of the effective Brillouin zone that respect $\mathcal{C}_2$- and $\Theta$-symmetry, the rotation-symmetric time-reversed channels of periodic and smooth Bloch waves $\Psi^{I,II}(\vec{q})$ along the boundary of the effective Brillouin zone $\partial EBZ$ can be chosen completely independent of the Bloch waves $\chi^{I,II}(\vec{q})$ in the interior of the EBZ, provided they make the $\mathcal{C}_2\Theta$ sewing matrix completely off-diagonal. We have therefore decomposed the task of finding a continuous, periodic, and rotation-symmetric set of time-reversed projectors $\rho^{I,II}(q)$ into two simpler, and computationally possible problems. Namely, the construction of a $\mathcal{C}_2\Theta$-symmetric gauge within the EBZ, and the construction of a $\mathcal{C}_2$ & $\Theta$-symmetric gauge along the boundary $\partial EBZ$. The winding number $W(\mathcal{U}|_{\partial EBZ})$ effectively reveals whether or not the gauge along $\partial EBZ$ can be matched with the gauge constructed within the EBZ. All in all, the following steps need to be implemented in order to compute the partial real-space invariants of a twofold rotation-symmetric crystal with time-reversal symmetry:

(i) construct a continuous and periodic $\mathcal{C}_2$ & $\Theta$-symmetric gauge of Bloch waves $\Psi(\vec{q})$ along $\partial EBZ$,

(ii) compute the partial Berry phase and the multiplicities of the rotation-symmetry eigenvalues using $\Psi(\vec{q})$,

(iii) construct a continuous, but not necessarily periodic, $\mathcal{C}_2\Theta$-symmetric gauge for Bloch waves $\chi(\vec{q})$ within the EBZ, and

(iv) compute the $\mathbb{Z}_2$- or $\mathbb{Z}$-winding number of the overlap-matrix $U(\vec{q}) = \langle\chi(\vec{q})|\Psi(\vec{q})\rangle$ along $\partial EBZ$.

Figure 2 sketches a computationally feasible strategy to perform the four steps mentioned above. We refer the reader to the Methods section for more details on the computational procedures in twofold rotation-symmetric crystals and Supplementary Note IV for the generalization to the case of $\mathcal{C}_4$- and $\mathcal{C}_6$-symmetric crystals.
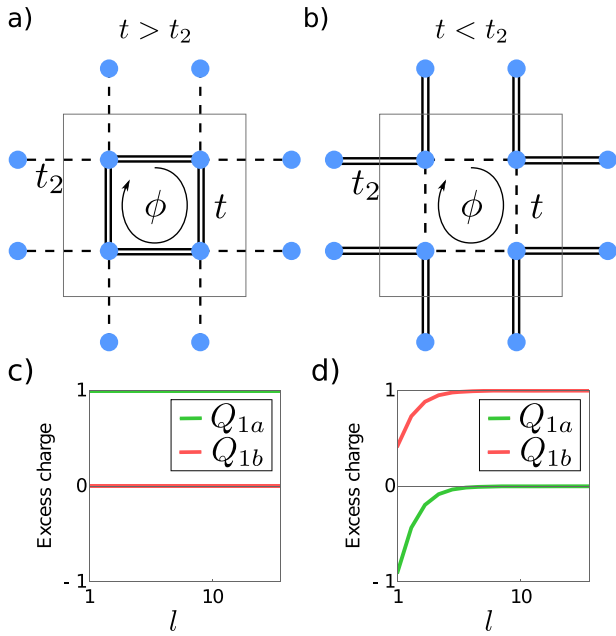
**Fig. 3 Quantized corner charges are not uniquely determined by Berry phases and crystalline symmetry eigenvalues. a)** Sketch of the Hamiltonian for one spin sector of the $\mathcal{C}_4$-symmetric system that realizes an atomic insulating phase at half-filling with two electrons at Wyckoff position $1a$ or **b)** $1b$ depending on the parameters. This model is adapted from ref. 58. **c)** Behavior of the corner charge density for the phase where two Kramers pairs are localized at $1a$ and **d)** $1b$ as obtained by increasing the $l \times l$ corner region size. Note that both phases have the same line invariants and symmetry eigenvalues.

## Relation to topological crystalline line invariants

We next discuss the relation between the partial real-space invariants defining the bulk-corner correspondence and the quantized partial polarizations – the so-called line invariants – along lines in the Brillouin zone that are mirror, or equivalently twofold-rotation, symmetric[29,30]. We recall that these $\mathbb{Z}_2$ invariants can be written in a $\mathcal{U}(N_F)$ invariant form that only requires a periodic gauge from numerically obtained eigenstates[30].

Let us consider, as before, the case of twofold rotation symmetric crystal [we refer the reader to Supplementary Note V for the $\mathcal{C}_{4,6}$ cases] and use that insisting on a gauge choice that makes the two time-reversed channels $\mathcal{C}_2$ symmetric the quantized partial polarization along the $k_2 = 0$ ($\Gamma - X$) line of the Brillouin zone (BZ) can be simply written as $\gamma_1^I = \Gamma_i^I + X_i^I$ modulo an even integer. Likewise, the quantized partial polarization along the $k_1 = 0$ ($\Gamma - Y$) line of the BZ reads $\gamma_1^I = \Gamma_i^I + Y_i^I$. Note that the quantized partial polarization on the $k_{1,2} = \pi$, i.e., the $Y - M$ and the $X - M$ lines respectively, are not independent since they are related to the polarization $\gamma_{1,2}^I$ via the $\mathbb{Z}_2$ topological invariant $\nu_{FKM}$ originally introduced by Fu, Kane, and Mele[6,7]. It is straightforward to show that the two independent $\mathbb{Z}_2$ line invariants can be immediately expressed in terms of the partial real-space invariants. Using that the latter are well-defined modulo 2 in a $\mathcal{C}_2$-symmetric crystal, and taking advantage of the compatibility relations for the $\mathcal{C}_2$ symmetry eigenvalues $HS_i + HS_{-i} \equiv N_F$ with $HS = \Gamma, X, Y, M$, we immediately find [Table 1] the following equalities modulo 2

$$\begin{aligned}(\nu_{1b}^I + \nu_{1d}^I) &= (\nu_{FKM} - \gamma_1^I),\\(\nu_{1c}^I + \nu_{1d}^I) &= (\nu_{FKM} - \gamma_2^I).\end{aligned} \quad (9)$$

Here, we have used the relation between the Chern number of the $I$, $II$ channels and the Fu–Kane–Mele invariant: $\nu_{FKM} = C^I \mod 2$. While partial real-space invariants uniquely determine the

topological crystalline line invariants, the opposite is not true. More generally, the fact that the line invariants do not resolve the bulk-corner correspondence can be seen by noticing that there is a single constraint on the $\nu_{1x}^I$ invariants modulo 2, namely

$$(\nu_{1a}^I + \nu_{1b}^I + \nu_{1c}^I + \nu_{1d}^I) = \Gamma_i^I - \Gamma_{-i}^I = \frac{N_F}{2}. \quad (10)$$

This also implies that for an arbitrary $N_F$ number of occupied bands, a $\mathcal{C}_2$- and $\Theta$-symmetric insulator can be characterized by three partial real-space $\mathbb{Z}_2$ indices, which, together with $\nu_{FKM}$, form a $\mathbb{Z}_2 \times \mathbb{Z}_2 \times \mathbb{Z}_2 \times \mathbb{Z}_2$ classification. This has clearly more topological content than the $\mathbb{Z}_2 \times \mathbb{Z}_2 \times \mathbb{Z}_2$ characterization in terms of line invariants and Fu–Kane–Mele invariants. Notice that the same holds true also in crystals with fourfold- and sixfold-rotation symmetries. This is simply because the corresponding $\mathbb{Z}_{4,6}$ quantized corner charges cannot be resolved by the $\mathbb{Z}_2$ quantized polarizations.

To prove concretely that the topological crystalline line invariants do not completely resolve the bulk-corner correspondence let us introduce a fourfold rotation-symmetric atomic insulating phase at $N_F = 4$ using the model schematically shown in Fig. 3. It can be thought of as being composed of two time-reversed copies of the spinless model introduced in ref. 58 with the two channels mixed by a spin–orbit coupling term. Specifically, we couple site 1 and 2 by a term $\lambda i \sigma_x$ and site 3 and 4 by a term $\lambda i \sigma_y$ within the unit cell, and set $\lambda = 0.3$. At half-filling, the insulating state realized for $|t/t_2| > 1$ and $\phi = -\pi$ [see Fig. 3a] has a simple decomposition in two channels with zero Chern number and $\nu_{1a}^I \equiv 1$; $\nu_{1b,2c}^I \equiv 0$. This is consistent with the explicit computation of the corner charge shown in Fig. 3c that shows $Q_{1a} = 1$ while $Q_{1b} = Q_{2c} = 0$. However, tuning the parameters to $|t/t_2| < 1$ and $\phi = \pi$ [see Fig. 3b], this model realizes a different set of real-space invariants $\nu_{1b}^I \equiv 1$; $\nu_{1a,2c}^I \equiv 0$. And indeed the charge density shown in Fig. 3d predicts $Q_{1b} = 1$ while $Q_{1a} = Q_{2c} = 0$. The change in charge density is however not detected by the line invariants that are vanishing in both spaces, i.e., $\gamma_1^I \equiv \gamma_2^I \equiv 0$. This is because the two insulating phases can be described in terms of two Wannier Kramers pairs centered either at the center $1a$ of the unit cell or at the $1b$ edge of the unit cell, which clearly give the same partial polarizations.

## Detecting the topology of quantum spin-Hall insulators

As mentioned above, the partial real-space invariants provide us with the bulk-corner correspondence in crystals that are insulating both in the bulk and along their edges. Therefore, they are ill-defined when dealing with quantum spin-Hall insulators due to the presence in the latter of helical edge states. This assertion, however, is only true when considering crystalline systems in isolation. Let us now instead consider one insulating system that is completely surrounded by a second insulator[59] as shown in Fig. 4a. For such a geometry, we define the corner charge of the combined system as the sum of the charge in the corner of the inner insulator and the charge in the L-shaped region of the surrounding insulator adjoining the first corner region. In addition, both regions will be measured with respect to a special Wyckoff position in order to ensure quantization of the corner charge. In the case of atomic and fragile topological insulators, inspection of the corner charge in this geometry does not provide any additional information. On the contrary, if the two insulators are of the quantum spin-Hall type, by computing the combined corner charge additional information on the crystalline topology can be extracted.

We recall that from an edge perspective all quantum spin-Hall insulators are topologically identical: the presence of the helical edge states is mandated by the non-trivial value of the Fu–Kane–Mele $\mathbb{Z}_2$ invariant. In $\mathcal{C}_n$-symmetric crystals, however, quantum spin-Hall phases can be additionally characterized by the
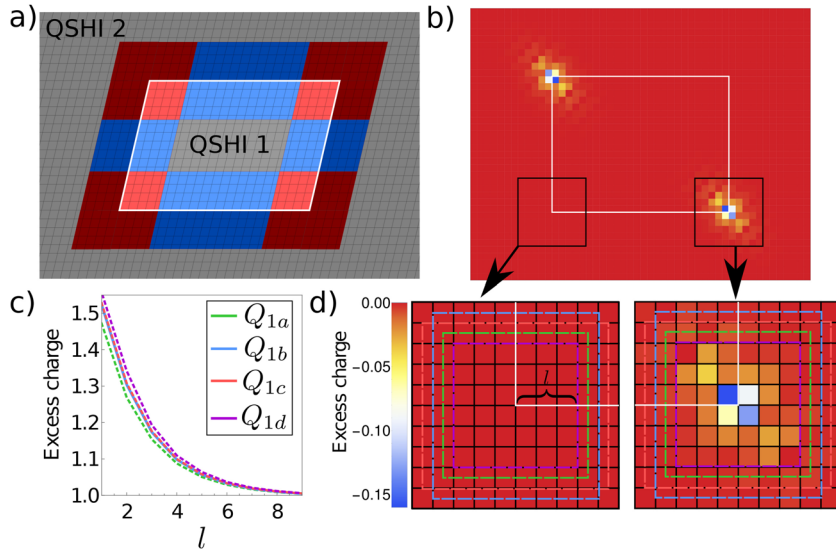
**Fig. 4 Quantized corner charges in quantum spin-Hall heterostructures. a)** Schematic of a $\mathcal{C}_2$ QSH system embedded in another QSH system with periodic boundary conditions. The edge and corner regions of the interface are colored blue and red, respectively. **b)** Corresponding charge density for the QSH systems discussed in the text. **c)** Behavior of the corner charge as a function of the $l \times l$ corner regions size. **d)** Zoom in of the charge density, depicting the two corners and the regions used to calculate the corner charges.

quantized partial Berry phases, and they can be revealed by the charge trapped at dislocation defects. As shown in ref. 39, however, quantum spin-Hall phases in twofold rotation symmetric crystals are endowed with an additional topological $\mathbb{Z}_2$ invariant, which cannot be probed at these topological defects. We will now show that the corner charge in the geometry of Fig. 4a is diagnosed precisely by this crystalline topological index.

To prove the assertion above, we use the Kane–Mele model, which, as before, will be considered on a uniaxially strained honeycomb lattice to remove the additional threefold rotation symmetry. Using the results of ref. 39, it can be shown that the quantum spin-Hall insulating phase realized choosing the nearest neighbor hopping amplitude $t = 1$ is topologically distinct from the insulating phase realized choosing the opposite sign of the hopping amplitude, even though the spin–orbit coupling $\lambda_{ISO}$ remains unchanged. Moreover, the two states share the same partial Berry phases and consequently cannot be discriminated by analyzing the charge trapped at dislocations. When using the two phases in the combined geometry of Fig. 4a, an explicit computation of the quantized values of the corner charge [see Figs. 4b–d] yields $Q_{1a,1b,1c,1d} = 1$, as opposed to the result one would get for a system composed of two quantum spin-Hall insulators with equal crystalline topological indices, i.e., $Q_{1a,1b,1c,1d} = 0$.

Even more importantly, the quantized corner charges can be straightforwardly obtained using the bulk formulation of the partial real-space invariants, whereas they cannot be read off from the line invariants. For a Kane–Mele model on a strained honeycomb lattice with the parameter set choice $(t, \lambda_{ISO}) = (1, 1)$ the twofold rotation-symmetric channel with Chern number $C^I = 1$ is characterized by the following set of rotation symmetry labels $\Gamma_i^I = X_i^I = Y_i^I = M_{-i}^I = 1$. In the Kane–Mele quantum spin-Hall phase with $(t, \lambda_{ISO}) = (-1, 1)$ the $I$ channel with $C^I = 1$ has reversed rotation symmetry labels $\Gamma_{-i}^I = X_{-i}^I = Y_{-i}^I = M_i^I = 1$. As a result, these two $\nu_{FKM} = 1$ systems cannot be distinguished by the values of the line invariants $\gamma_1^I \equiv \gamma_2^I \equiv 0$. However, the $\nu_{1x}^I$ are manifestly different. In fact, using the expressions listed in Table 1 the first Kane–Mele model has $\nu_{1a}^I = \nu_{1b}^I = \nu_{1c}^I \equiv 1$ and $\nu_{1d}^I = 0$ while these invariants are reversed by switching the hopping amplitude sign, i.e.,$\nu_{1a}^I = \nu_{1b}^I = \nu_{1c}^I \equiv 0$ and $\nu_{1d}^I = 1$. Note that the quantized corner charges in the heterostructure containing both

quantum spin-Hall insulators, $Q_{1x} = \Delta\nu_{1x}^I \equiv 1$, are consistent with the direct real-space calculation of Fig. 4c, d.
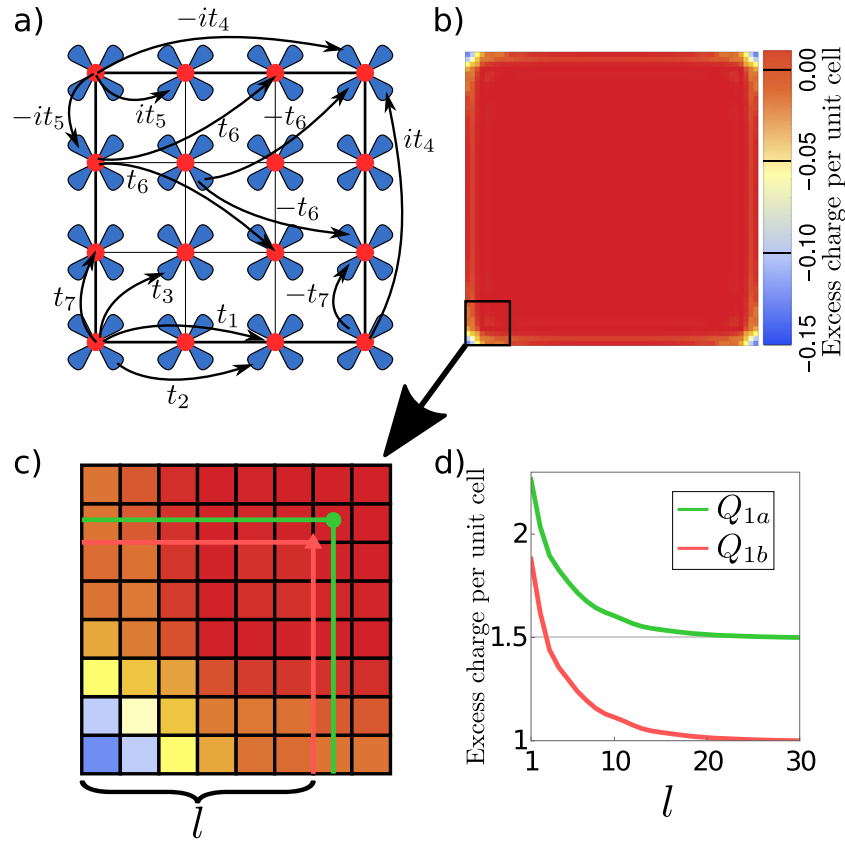
Quantized corner charges as a probe of fragile topology

Next, we will show that the partial real-space invariants represent a powerful diagnostic tool to detect fragile topological phases. As mentioned above, the absence of gapless edges guarantees that topological fragile phases do possess quantized corner charges that are in a one-to-one correspondence with the partial real-space invariants. In the following, we will derive an inequality that the set of partial real-space invariants necessarily satisfies if the insulator is an atomic one. Consequently, a violation of this inequality indicates that the system must be a fragile topological insulator as long as its edges are insulating.

Let us first introduce for each special Wyckoff position the positive integer quantities directly related to the partial real-space invariants $\bar{\nu}_{mx}^I = \nu_{mx}^I \mod (n/m)$. The $\bar{\nu}_{mx}^I$'s can be immediately related via an exact equality to the quantized part of the corner charges, namely $Q_{mx} = 2\bar{\nu}_{mx}^I m/n$. Even more importantly, for an insulating phase adiabatically connected to an atomic limit the $\bar{\nu}_{mx}^I$ represent lower bounds for the number of exponentially localized Wannier functions with center of charge coinciding with the special Wyckoff positions $N_{mx} \geq 2\bar{\nu}_{mx}^I$. Furthermore, the total number of electrons in the unit cell satisfies $N_F \geq \sum m \times N_{mx}$ where the sum runs over all the special Wyckoff positions in the unit cell of the rotation symmetric crystal. Combining these two inequalities allows us to derive the following condition fulfilled by a generic atomic insulating phase $N_F \geq \sum 2\, m \times \bar{\nu}_{mx}^I$. Insulating phases for which this inequality is violated do not allow an adiabatic deformation to an atomic limit, and hence correspond to fragile topological insulators. We can encode this criterion in a discriminant

$$\mathcal{D}_{\mathcal{C}_n} = N_F - \sum 2\, m \times \bar{\nu}_{mx}^I, \tag{11}$$

where, as before, the sum runs over all special Wyckoff positions in the unit cell of the rotation-symmetric crystal. A negative value of $\mathcal{D}_{\mathcal{C}_n}$ implies the existence of a topological obstruction in deforming the insulating phase to an atomic limit, and consequently a fragile topological nature. We remark that the criterion for the topological non-triviality of a fragile phase cannot be read off from the values of the partial real-space invariants

**Fig. 5 Fragile topological phases and their quantized corner charges. a)** Schematic drawing of the hopping parameters for one spin sector of the $\mathcal{C}_4$ symmetric fragile topological insulator model. **b)** Charge density of a $\mathcal{C}_4$ symmetric fragile topological insulator for a square sample of 60 by 60 unit cells. **c)** Charge density of the lower left corner. The sum of the charge in the red and green areas give the corner charges $Q_{1a}$ and $Q_{1b}$, respectively. **d)** Corner charges as a function of the size of the summed region $l$. The corner charges exponentially go to the values of 1.5 and 1. Charge density is calculated for $t_1 = 0.25$, $t_2 = -0.4$, $t_3 = 0.55$, $t_4 = -0.35$, $t_5 = -0.56$, $t_6 = 0.125$, $t_7 = 0.25$.

taken by themselves. It is instead stored in a single $\mathbb{Z}_2$ invariant corresponding to the sign of the discriminant $\mathcal{D}_{\mathcal{C}_n}$.

We now demonstrate the diagnostic capability of this discriminant, and consider a concrete realization of a fragile phase in a $\mathcal{C}_4$-symmetric crystal. The model is schematically shown in Fig. 5a and is defined on a square lattice, with each-unit cell hosting one $s$-like and one $d$-like orbital. Besides conventional nearest-neighbor hoppings we have also included fairly strong long-range hopping processes. At half-filling both the bulk and the edges of this system are completely insulating [see Supplementary Note VI], which implies that the corner charges are well-defined and quantized. Explicit computation of the corner charges in the open geometry of Figs. 5b–d yields the following results: $Q_{1a} = 3/2$, $Q_{1b} = 1$, and $Q_{2c} = 0$. This is in agreement with the computation of the bulk partial real-space invariants that can be easily performed decomposing the time-reversal invariant insulator in two time-reversed Chern insulator with channel Chern number $C^{I,II} = \pm 4$ [see Supplementary Note VI]. Using the expression for the real-space invariants listed in Table 1, we indeed find $\bar{\nu}^I_{1a} = 3$, $\bar{\nu}^I_{1b} = 2$, and $\bar{\nu}^I_{2c} = 0$. Moreover, since at half-filling only one pair of Kramers related bands are occupied, i.e., $N_F = 2$, we have that the discriminant $\mathcal{D}_{\mathcal{C}_4} = -8$, thus signaling a fragile topological insulating nature.

We corroborate this finding by verifying the hallmark of fragile topological insulators—the decay into an atomic insulating state by addition of certain topologically trivial electronic bands. Consider, for instance, the addition of a single Kramers' related pair of bands. To preserve the fourfold rotation symmetry, the added atomic bands will either correspond to a localized Wannier Kramers' pair centered at the origin of the unit cell 1$a$, or at the

corner of the unit cell 1$b$. In the latter case, we find that $\bar{\nu}^I_{1b} = 3$ whereas $\bar{\nu}^I_{1a,2c}$ remain unaffected. This increase in the corner charge $Q_{1b}$ is exactly compensated by the change of $N_F = 2 \rightarrow 4$ in the discriminant $\mathcal{D}_{\mathcal{C}_4}$ that consequently remains negative indicating that the system is not trivialized. Let us now consider the addition of a Wannier Kramers pair localized at 1$a$. This implies that $\bar{\nu}^I_{1a}$ is modified according to $\bar{\nu}^I_{1a} = 3 \rightarrow 0$ while the other topological crystalline invariants remain unchanged. This consequently implies a change in the discriminant $\mathcal{D}_{\mathcal{C}_4} = -8 \rightarrow 0$, which verifies the decay of the fragile topological insulator into a conventional atomic insulator.

It is important to point out that in a $\mathcal{C}_4$ ($\mathcal{C}_6$) symmetric crystal the presence of the twofold rotation symmetry allows one to simultaneously define also a $\mathcal{D}_{\mathcal{C}_2}$ discriminant [see Supplementary Note VII]. A negative value of this discriminant automatically implies a negative value for $\mathcal{D}_{\mathcal{C}_4}$ ($\mathcal{D}_{\mathcal{C}_6}$). However, the converse needs not to be true. This is verified, for instance, in the model of Fig. 5a where an electron pair is added at the 1$b$ corner of the unit cell. The fourfold rotation discriminant $\mathcal{D}_{\mathcal{C}_4} = -8$ implies fragile topology whereas the $\mathcal{C}_2$ specific discriminant $\mathcal{D}_{\mathcal{C}_2}$ identically vanishes and on the contrary would signal an atomic insulator. This property implies that the fragile topology of this model cannot be seen using diagnostic tools specifically designed for twofold rotation symmetric systems, as for instance, the Wilson-loop based indices developed in refs [45,60,61]. Furthermore, the fact that the fragile topology relies purely on the fourfold rotation symmetry, implies that a structural orthorhombic distortion also yields an electronic topological phase transition to an atomic insulating phase.

Finally, we point out that in $C_2$-symmetric crystals all insulating phases are atomic for $N_F \geq 6$: this is because $\bar{v}^i_{1x} = 0, 1$ and consequently the discriminant has an upper bound for an even number of Kramers' related pairs of bands $\mathcal{D}_{C_2} \geq N_F - 8$ while for an odd number of pairs of bands $\mathcal{D}_{C_2} \geq N_F - 6$. On the contrary, the existence of $C_4$-protected fragile topological phases is not limited to systems with two occupied pairs of Kramers' related bands. If starting out from the model in Fig. 5a we would consider the addition of two Wannier Kramers' pairs centered at the two Wyckoff positions $2c$, the change in $N_F = 2 \rightarrow 6$ would be exactly compensated by the increase in $\bar{v}^i_{2c} = 0 \rightarrow 1$ that leaves the discriminant unaltered.

## DISCUSSION

In short, we have introduced the gauge-invariant crystalline topological indices that govern the quantized corner charges present in two-dimensional rotation symmetric insulators with time-reversal symmetry. We dubbed these topological integers partial real-space invariants. They cannot be expressed in terms of Wilson loop invariants, partial Berry phases or symmetry-based indicators: their computation requires a completely different approach that we have developed throughout our work. Beside defining the bulk-corner correspondence of conventional band insulators adiabatically connected to an atomic limit, the partial real-space invariants can be used to unveil the crystalline topology of quantum spin-Hall insulators, and represent a unique tool to diagnose the recently discovered topological phases of the fragile type in time-reversal symmetric crystals. The bulk-corner correspondence formulated in this work is capable of detecting all fragile topological phases in systems with spin-orbit coupling and time-reversal symmetry.

## METHODS

### $C_2$ & $\Theta$-symmetric gauge along the effective BZ boundary

In order to construct a continuous, $C_2$- and $\Theta$-symmetric gauge along the boundary of the effective Brillouin zone, we develop a procedure inspired by the parallel-transport procedure developed in ref. [62]. The procedure can be divided in three steps and is sketched in Fig. 2.

*Step 1:* At the four high-symmetry momenta $HS \in \{\Gamma = (0, 0), Y = (0, \pi), M = (\pi, \pi) X = (\pi, 0)\}$ we pick $N_F$ Bloch states $|\chi_{t.s.}(HS)\rangle$ in a gauge that is $C_2$ and $\Theta$-symmetric. In the following, we refer to these states at the high-symmetry points of the EBZ as target states. We point out that such a set of states can be easily constructed by diagonalizing the $C_2$ symmetry operator.

*Step 2:* Having selected the target states at the four high-symmetry points in the Brillouin zone, we next have to find a continuous gauge that joins the target states along the upper half of $\partial EBZ$ while simultaneously preserving the off-diagonal structure of the $C_2\Theta$ sewing matrix. Let us first consider the line connecting $\Gamma - Y$, and define an equally spaced mesh $\vec{q}_j = (0, q_{j,y})$ with $j = 0, \ldots, \mu$ such that $q_{0,y} = 0$ and $q_{\mu,y} = \pi$. We initialize the parallel transported states by defining the $N_F$ states at $\Gamma$ as $|\chi_{p.t.}(\vec{q}_0)\rangle := |\chi_{t.s.}(\Gamma)\rangle$. We can then define the parallel transported states over the entire mesh using the following iterative procedure: starting from the parallel-transported states $|\chi_{p.t.}(\vec{q}_j)\rangle$, we uniquely determine the parallel-transported states at $|\chi_{p.t.}(\vec{q}_{j+1})\rangle$ by requiring the overlap matrix $\mathcal{M}(\vec{q}_j, \vec{q}_{j+1}) = \langle \chi_{p.t.}(\vec{q}_j)|\chi_{p.t.}(\vec{q}_{j+1})\rangle$ to be Hermitian and with only positive eigenvalues. This can be accomplished by employing a singular value decomposition. Starting from an arbitrary gauge at $\vec{q}_{j+1}$, we write the overlap matrix $\widetilde{\mathcal{M}}(\vec{q}_j, \vec{q}_{j+1}) = \langle \chi_{p.t.}(\vec{q}_j)|\chi(\vec{q}_{j+1})\rangle$ as $\widetilde{\mathcal{M}} = V\Sigma W^\dagger$, with $V$ and $W$ unitary matrices and $\Sigma$ a postive real diagonal matrix. The parallel-transported states are defined by the unitary transformation of the $|\chi(\vec{q}_{j+1})\rangle$ states as $|\chi_{p.t.}(\vec{q}_{j+1})\rangle = WV^\dagger|\chi(\vec{q}_{j+1})\rangle$. This guarantees that the modified overlap matrix $\mathcal{M} = V\Sigma V^\dagger$ is Hermitian and positive. This iterative procedure can be repeated until we have arrived at $(0, \pi) = Y$. Moreover, the parallel transport procedure ensures that the block diagonal form of the $C_2\Theta$ sewing matrix, or equivalently the constraint

$|\chi^{II}_{p.t.;m}(\vec{q}_j)\rangle = C_2\Theta|\chi^I_{p.t.;m}(\vec{q}_j)\rangle$, is satisfied along the entire line [this is shown in Supplementary Note VIII].

This, however, is not yet the end of the story: by definition, the parallel transported states at $\Gamma$ coincide with the target state. The same, however, does not hold true at the $Y$ point: the parallel-transported states $|\chi_{p.t.}(Y)\rangle$ will generically not be equal to the target states selected at $Y$. In order to correct this, we can in principle apply a residual gauge transformation $U(\vec{q}_j)$ to rotate the parallel-transported states $|\chi_{p.t.}(\vec{q}_j)\rangle \rightarrow U(\vec{q}_j)|\chi_{p.t.}(\vec{q}_j)\rangle$. Specifically, the residual gauge transformation should interpolate between the identity matrix at $\Gamma$ and $\mathcal{M}^*_Y = \langle \chi_{t.s}(Y)|\chi_{p.t.}(Y)\rangle^*$ at $Y$. With a continuous and smooth residual gauge transformation, this is only possible if the identity matrix and $\mathcal{M}^*_Y$ belong to the same connected component of the subgroup $U(N_F)_{C_2\Theta}$. Put differently, the determinant of $\mathcal{M}^*_Y$ has to be $+1$. Assuming the determinant is instead equal to $-1$, we cannot use any residual gauge transformation to connect our target states at $\Gamma$ and $Y$. However, in this case we have the freedom to redefine the target states selected at $Y$, by exchanging a single state from sector $I$ with its Kramers partner in sector $II$. This will switch the sign of the $\mathcal{M}^*_Y$ determinant and eventually allow to interpolate our target states. In concrete terms, we will apply the following residual gauge transformation: $|\chi(\vec{q}_j)\rangle \rightarrow \exp(q_{j,y}\log(\mathcal{M}^*_Y)/\pi)|\chi(\vec{q}_j)\rangle$. To ensure that the states transformed with this additional residual gauge transformation still obey the symmetry constraint $|\chi^{II}_{p.t.;m}(\vec{q}_j)\rangle = C_2\Theta|\chi^I_{p.t.;m}(\vec{q}_j)\rangle$, we take the logarithm that takes values within the Lie algebra of $U(N_F)_{C_2\Theta}$. Specifically, denoting the eigenvalues and eigenvectors of $\mathcal{M}^*_Y$ by $e^{i\theta_j}$ and $v_j$, with $j = 1, \ldots, N_F$, one can express this logarithm as $\log(\mathcal{M}^*_Y) = \sum_j i\theta_j v_j v_j^\dagger$, where we require that $\theta_j \in (-\pi, \pi)$, and for simplicity we have assumed that all of the eigenvalues are distinct. With this, we finally obtain a continuous gauge along the line connecting $\Gamma$ and $Y$, which gives as output the $C_2$-symmetric time-reversed target states selected at $\Gamma$ and $Y$ while simultaneously keeping the block off-diagonal structure of the $C_2\Theta$ symmetric sewing matrix. Next, we repeat the above steps along the line connecting $Y$ and $M$, and the line connecting $M$ and $X$, to find our continuous, smooth, and symmetric gauge along the upper half of $\partial EBZ$.

*Step 3:* Finally, we need to extend the gauge found at *Step 2* to the entire boundary of the effective Brillouin zone. Let us first consider the line connecting $\Gamma$ and $-Y = (0, -\pi)$. We can define $|\chi(\vec{q})\rangle$ for $-\pi < q_{j,y} < 0$ as follows:

$$|\chi^a_m(\vec{q}_j)\rangle := -\exp(q_{j,y}(Y^a_m - \Gamma^a_m)/2)\Gamma^a_m C_2|\chi^a_m(-\vec{q}_j)\rangle, \tag{12}$$

where $Y^a_m$ and $\Gamma^a_m$ denote the $C_2$ eigenvalues of the target states at $Y$ and $\Gamma$, respectively. Note that the prefactor $-\exp(q_{j,y}(Y^a_m - \Gamma^a_m)/2)\Gamma^a_m$ ensures that the gauge in the negative half of $\partial EBZ$ matches the gauge in the positive half. Next, we can implement this procedure in an analogous way along the line connecting $X$ and $-M = (\pi, -\pi)$. The gauge along the line connecting $Y$ and $M$ in the lower half can be instead simply taken to be equal to the section connecting $Y$ and $M$ in the upper half.

### Computing the Berry phase and $C_2$ symmetry labels

With our continuous and $C_2$ & $\Theta$–symmetric gauge along the effective Brillouin zone boundary in our hands, we can straightforwardly compute the (partial) Berry phase contribution as well as the multiplicities entering the $v^i_{1x}$ expressions of the topological invariants. To compute in particular the Berry phase contribution let $\vec{q}_j$ with $j = 0, \ldots, \mu$ parametrize the mesh along the effective Brillouin zone boundary. Then, using the gauge found in the previous step, we have

$$\oint_{\partial EBZ} d\vec{q} \cdot Tr(\vec{A}^I(\vec{q})) = \sum_j \text{Im}(\log(\det(\mathcal{M}^I(\vec{q}_j, \vec{q}_{j+1})))), \tag{13}$$

with $\mathcal{M}^I(\vec{q}_j, \vec{q}_{j+1})_{m,n} = \langle \chi^I_m(\vec{q}_j)|\chi^I_n(\vec{q}_{j+1})\rangle$ the overlap matrix between states at adjacent momenta. Note that this expression does return the Berry phase for the gauge that we have constructed, i.e., the equality is a true equality (not modulo $2\pi$).

### Constructing a $C_2\Theta$-symmetric gauge in the effective BZ

In order to obtain a continuous $C_2\Theta$-symmetric gauge in the effective Brillouin zone, we employ again a parallel transport procedure We initialize our procedure by selecting at the lower-left corner of the effective Brillouin zone, the $-Y = (0, -\pi)$ point, a set of Bloch states such that the

$C_2\Theta$-constraint $|\chi^{II}_{p.t.:m}(\vec{q}_j)\rangle = C_2\Theta|\chi^{I}_{p.t.:m}(\vec{q}_j)\rangle$ is obeyed, see Fig. 2i. Next, we use the iterative parallel transport procedure in the $\hat{q}_y$-direction to obtain a $C_2\Theta$-symmetric gauge along the left edge of the effective Brillouin zone, see Fig. 2j. We thereafter use each point along this line as a starting point to iterate the parallel transport of these Bloch states into the $\hat{q}_x$-direction. This is illustrated in Fig. 2k, d. Upon completion of these steps, we find a continuous $C_2\Theta$-symmetric gauge in the entire effective Brillouin zone.

### Computing the $\mathbb{Z}_2$ winding number of $\mathcal{U}_{C_2\Theta}(N_F)$

To show how to compute the winding number of the overlap matrix $\mathcal{U} = \langle\chi(\vec{q})|\Psi(\vec{q})\rangle$, we recall that as shown in Supplementary Note III the group of $C_2\Theta$-preserving gauge transformations is conjugate to the orthogonal group. It is also instructive to remember that the logarithm of a non-zero complex number $z = \rho e^{i\theta}$, with $\rho \in \mathbb{R}_+$ and $\theta \in \mathbb{R}$ is a multi-valued function: the logarithm $\log(z)$ is only well-defined up to integer multiples of $2\pi i$. A simple way to define a proper single-valued function is to require the imaginary part of the logarithm to take values in the open interval $(-\pi, \pi]$. One refers to such a logarithm as the principal logarithm.

We can now analogously define the principal logarithm of an element of the special orthogonal group. First, we consider for simplicity the special orthogonal group in two dimensions. Let $M \in SO(2)$, and denote its two eigenvectors as $v_1$ and $v_2$, with corresponding eigenvalues $e^{i\theta_1}$ and $e^{i\theta_2}$. Since $M$ is a real unitary matrix, the following relation must hold $e^{i\theta_2} = e^{-i\theta_1}$. Moreover, the eigenvectors $v_1$ and $v_2$ are related to each other by complex conjugation (in the rare event that $\theta = 0, \pi$ this might require a basis transformation). It is therefore natural to define the principal logarithm of the matrix $M$ as follows:

$$\log(M) := i\theta_1 v_1 v_1^\dagger + c.c. = \theta_1 X_1, \text{ with } \theta_1 \in (-\pi, \pi], \tag{14}$$

and where $c.\,c.$ denotes the complex conjugate. In this way, we can transform the multi-valued logarithm into a single-valued function as long as $\theta_1 \neq \pi$. In fact, for $\theta_1 = \pi$ there is an intrinsic ambiguity in the definition of the principal logarithm since we could freely replace $v_1$ by $v_2$. We can however remedy to this ambiguity by requiring that in the expression for the principal logarithm $v_1 := (1, +i)^T$. With this, we can conclude that there is a one-to-one mapping between $SO(2)$ and $U(1)$. In particular, this implies that their fundamental homotopy groups coincide: $\pi_1(SO(2)) = \pi_1(U(1)) = \mathbb{Z}$. We can straightforwardly determine the $\mathbb{Z}$-number associated to an element of $SO(2)$ on a loop by counting the number of times $n_+$ the logarithm crosses its branch cut clockwise, and subtracting to it number of times $n_-$ the branch cut is crossed anti-clockwise. In practice, one counts the number of times that the principal logarithm makes a sudden jump by $+2\pi i\sigma_y$ and the number of times it jumps by $-2\pi i\sigma_y$. Note that $n_+$ and $n_-$ are individually not invariant, as an anti-clock wise crossing can annihilate a clock-wise crossing.

We next generalize the results above to $SO(N)$ with $N > 2$, assuming for simplicity $N$ to be even. Using the sorted real Schur decomposition discussed in ref. [63], we can group the eigenvectors and eigenvalues into $N/2$ pairs $v_{2j-1}$ and $v_{2j}$, and corresponding eigenvalues $e^{\pm i\theta_j}$. With this, we thereafter define the principal logarithm as:

$$\log(M) := \sum_{j=1}^{N/2} i\theta_j v_{2j-1} v_{2j-1}^\dagger + c.c. = \sum_{j=1}^{N/2} \theta_j X_j, \tag{15}$$

where $X_j$ is a skew-symmetric matrix with $\langle\langle X_i, X_j\rangle\rangle = \text{Tr}(X_i^T X_j) = 2\delta_{i,j}$, and $\theta_j \in (-\pi, \pi]$ for $j = 1, \ldots, N/2$. Precisely as for the $SO(2)$ case, the principal logarithm is uniquely defined as long as $\theta_j \neq \pi \forall j$. However, in this case we cannot resolve the ambiguity if one of the angles $\theta_j = \pi$. This difference can be understood as follows. A $n$-dimensional rotation with $n > 2$ can be represented as for the two-dimensional case with pairs of oriented planes, here given by $X_j$, and corresponding angles $\theta_j$. In the two-dimensional case, it is possible to resolve the ambiguity for $\theta = \pi$, since the orientation of a two-dimensional plane can be globally specified. This does not hold for higher-dimensional rotation because the oriented planes can be rotated. Such a detail has major consequences for the fundamental homotopy group of $SO(N)$ for $N > 2$. Namely, we can no longer distinguish between a logarithm that crosses the branch cut in a clock-wise or anti clockwise direction. Instead, we can only consider the total number of crossings $n$, which is a quantity determined up to multiples of two since, as mentioned above crossings can be annihilated in pairs. Put in simple terms, the fundamental group of $SO(N)$ is given by $\mathbb{Z}_2$ if $N > 2$.

We now present an explicit numerical recipe to determine whether or not a loop in $SO(N)$ is null-homotopic. Assume that we are given a set set of orthogonal matrices $M(i)$ with $i = 1, \ldots, L$, satisfying the constraint $\|M(i) - M(i+1)\| \ll 1$. Furthermore, we require that the set of matrices form a closed loop, i.e. $M(L) = M(1)$. As a first step, we compute the principal logarithm for each of the $L$ matrices, ensuring that $\log(M(L)) = \log(M(0))$ to respect the periodicity. We can compute the principal logarithm using the following Python code:

```
import numpy as np
from scipy.linalg import schur, eigvals, expm
def principalLog(M):
  """
  :input M: special orthogonal matrix of even
dimension Nf
  :output X0: skew-symmetric matrix of dimension N x N, s.
t. exp(X0)=M, and X0 = theta_i * X_i, with theta_i in [-pi,
pi]"""
  T, Z = schur(M)
  sort_real_schur(Z, T, 1.,0,inplace=True)
  Nf = len(M)
  X0 = np.zeros((Nf,Nf))
  for i in range(Nf//2):
  u = Z[:,2*i:2*i+1]
  v = Z[:,2*i+1:2*i+2]
  x =u*v.T - v*u.T
  theta = np.arctan2(T[2*i,2*i+1], \
  T[2*i,2*i])
  X0 += theta * x.copy()
  return X0
```

Here, we used the function sort_real_schur, an implementation of the real Schur decomposition of ref. [63], which can be found at https://gist.github.com/fabian-paul/14679b43ed27aa25fdb8a2e8f021bad5.

Having computed the principal logarithms, we next need to count the total number of branch cut crossings. To this end, we construct a function that returns the number of crossings between two nearby orthogonal matrices. Specifically, it uses that for two nearby orthogonal matrices $\|\log(M(i)) - \log(M(i+1))\|^2 \approx n \times 8\pi^2$, with $n$ the number of crossings in between. Typically $n$ will be equal to 0 or 1. This can be implemented in Python as follows:

```
def crossingIndicator(M1,M2):
  """M1 and M2 two nearby orthogonal matrices.
Returns n if n 2x2 blocks of the Schur decomposi-
tion cross the branch-cut of the logarithm.
  """
  L1 = principalLog(M1)
  L2 = principalLog(M2)
  delta = L2-L1
  k = np.linalg.norm(delta/(2*np.pi),ord=,-
fro,)**2/2
  k = round(k)
  return k
```

Finally, we need to sum the number of crossing over all neighboring points along the mesh. Here, we can use the following function:

```
def Z2(listM):
  """listM is a list of orthogonal matrices M(i).
  Returns the parity of the number of times the
branch-cut is crossed"""
  nu = 0
  for i in range(len(listM)-1):
  nu+= crossingIndicator(listM[i],listM[i+1])
  nu+=crossingIndicator(listM[-1],listM[0])
  return nu
```

## REFERENCES

1. Hasan, M. Z. & Kane, C. L. Colloquium: topological insulators. *Rev. Mod. Phys.* **82**, 3045–3067 (2010).

2. Qi, X.-L. & Zhang, S.-C. Topological insulators and superconductors. *Rev. Mod. Phys.* **83**, 1057–1110 (2011).

3. Thouless, D. J., Kohmoto, M., Nightingale, M. P. & den Nijs, M. Quantized Hall conductance in a two-dimensional periodic potential. *Phys. Rev. Lett.* **49**, 405 (1982).

4. Halperin, B. I. Quantized Hall conductance, current-carrying edge states, and the existence of extended states in a two-dimensional disordered potential. *Phys. Rev. B* **25**, 2185 (1982).

5. Kane, C. L. & Mele, E. J. Quantum spin Hall effect in graphene. *Phys. Rev. Lett.* **95**, 226801 (2005).

6. Kane, C. L. & Mele, E. J. $\mathbb{Z}_2$ topological order and the quantum spin Hall effect. *Phys. Rev. Lett.* **95**, 146802 (2005).

7. Fu, L. & Kane, C. L. Time reversal polarization and a $\mathbb{Z}_2$ adiabatic spin pump. *Phys. Rev. B* **74**, 195312 (2006).

8. Bernevig, B. A., Hughes, T. L. & Zhang, S.-C. Quantum spin Hall effect and topological phase transition in HgTe quantum wells. *Science* **314**, 1757–1761 (2006).

9. König, M. et al. Quantum spin Hall insulator state in HgTe quantum wells. *Science* **318**, 766–770 (2007).

10. Fu, L., Kane, C. L. & Mele, E. J. Topological insulators in three dimensions. *Phys. Rev. Lett.* **98**, 106803 (2007).

11. Moore, J. E. & Balents, L. Topological invariants of time-reversal-invariant band structures. *Phys. Rev. B* **75**, 121306 (2007).

12. Fu, L. & Kane, C. L. Topological insulators with inversion symmetry. *Phys. Rev. B* **76**, 045302 (2007).

13. Zhang, H. et al. Topological insulators in $Bi_2Se_3$, $Bi_2Te_3$ and $Sb_2Te_3$ with a single Dirac cone on the surface. *Nat. Phys.* **5**, 438 (2009).

14. Rasche, B. et al. Stacked topological insulator built from bismuth-based graphene sheet analogues. *Nat. Mat.* **12**, 422 (2013).

15. Xia, Y. et al. Observation of a large-gap topological-insulator class with a single Dirac cone on the surface. *Nat. Phys.* **5**, 398–402 (2009).

16. Fu, L. Topological crystalline insulators. *Phys. Rev. Lett.* **106**, 106802 (2011).

17. Hsieh, T. H. et al. Topological crystalline insulators in the SnTe material class. *Nat. Commun.* **3**, 982 (2012).

18. Hsieh, T. H., Liu, J. & Fu, L. Topological crystalline insulators and Dirac octets in antiperovskites. *Phys. Rev. B* **90**, 081112 (2014).

19. Liu, J. et al. Spin-filtered edge states with an electrically tunable gap in a two-dimensional topological crystalline insulator. *Nat. Mat.* **13**, 178 (2014).

20. Sessi, P. et al. Robust spin-polarized midgap states at step edges of topological crystalline insulators. *Science* **354**, 1269–1273 (2016).

21. Fang, C. & Fu, L. New classes of topological crystalline insulators having surface rotation anomaly. *Sci. Adv.* **5**, eaat2374 (2019).

22. Schindler, F. et al. Higher-order topological insulators. *Sci. Adv.* **4**, eaat0346 (2018).

23. Schindler, F. et al. Higher-order topology in bismuth. *Nat. Phys.* **14**, 918 (2018).

24. van Miert, G. & Ortix, C. Higher-order topological insulators protected by inversion and rotoinversion symmetries. *Phys. Rev. B* **98**, 081110 (2018).

25. Khalaf, E. Higher-order topological insulators and superconductors protected by inversion symmetry. *Phys. Rev. B* **97**, 205136 (2018).

26. Kooi, S. H., Van Miert, G. & Ortix, C. Inversion-symmetry protected chiral hinge states in stacks of doped quantum hall layers. *Phys. Rev. B* **98**, 245102 (2018).

27. Khalaf, E., Po, H. C., Vishwanath, A. & Watanabe, H. Symmetry indicators and anomalous surface states of topological crystalline insulators. *Phy. Rev. X* **8**, 031070 (2018).

28. Vanderbilt, D. & King-Smith, R. Electric polarization as a bulk quantity and its relation to surface charge. *Phys. Rev. B* **48**, 4442 (1993).

29. Lau, A., van den Brink, J. & Ortix, C. Topological mirror insulators in one dimension. *Phys. Rev. B* **94**, 165164 (2016).

30. van Miert, G. & Ortix, C. Excess charges as a probe of one-dimensional topological crystalline insulating phases. *Phys. Rev. B* **96**, 235130 (2017).

31. van Miert, G. & Ortix, C. Dislocation charges reveal two-dimensional topological crystalline invariants. *Phys. Rev. B* **97**, 201111 (2018).

32. Benalcazar, W. A., Li, T. & Hughes, T. L. Quantization of fractional corner charge in $C_n$-symmetric higher-order topological crystalline insulators. *Phys. Rev. B* **99**, 245151 (2019).

33. Li, T., Zhu, P., Benalcazar, W. A. & Hughes, T. L. Fractional disclination charge in two-dimensional $C_n$-symmetric topological crystalline insulators. *Phys. Rev. B* **101**, 115115 (2020).

34. Watanabe, H. & Ono, S. Corner charge and bulk multipole moment in periodic systems. *Phys. Rev. B* **102**, 165120 (2020).

35. Liu, Y. et al. Experimental discovery of bulk-disclination correspondence. Preprint at https://arxiv.org/abs/2003.08140 (2020).

36. Peterson, C. W., Li, T., Jiang, W., Hughes, T. L. & Bahl, G. Observation of trapped fractional charge and topological states at disclination defects in higher-order topological insulators. Preprint at https://arxiv.org/abs/2004.11390 (2020).

37. Peterson, C. W., Li, T., Benalcazar, W. A., Hughes, T. L. & Bahl, G. A fractional corner anomaly reveals higher-order topology. *Science* **368**, 1114–1118 (2020).

38. Pham, T. et al. Emergence of topologically nontrivial spin-polarized states in a segmented linear chain. *Phys. Rev. Lett.* **124**, 206403 (2020).

39. Kooi, S. H., van Miert, G. & Ortix, C. Hybrid-order topology of weak topological insulators. *Phys. Rev. B* **102**, 041122 (2020).

40. Bradlyn, B. et al. Topological quantum chemistry. *Nature* **547**, 298 (2017).

41. Po, H. C., Vishwanath, A. & Watanabe, H. Symmetry-based indicators of band topology in the 230 space groups. *Nat. Commun.* **8**, 50 (2017).

42. Zhang, T. et al. Catalogue of topological electronic materials. *Nature* **566**, 475 (2019).

43. Vergniory, M. et al. A complete catalogue of high-quality topological materials. *Nature* **566**, 480 (2019).

44. Tang, F., Po, H. C., Vishwanath, A. & Wan, X. Comprehensive search for topological materials using symmetry indicators. *Nature* **566**, 486 (2019).

45. Kooi, S. H., van Miert, G. & Ortix, C. Classification of crystalline insulators without symmetry indicators: atomic and fragile topological phases in twofold rotation symmetric systems. *Phys. Rev. B* **100**, 115160 (2019).

46. Schindler, F. et al. Fractional corner charges in spin-orbit coupled crystals. *Phys. Rev. Res.* **1**, 033074 (2019).

47. Bouhon, A., Black-Schaffer, A. M. & Slager, R.-J. Wilson loop approach to fragile topology of split elementary band representations and topological crystalline insulators with time-reversal symmetry. *Phys. Rev. B* **100**, 195135 (2019).

48. Bradlyn, B., Wang, Z., Cano, J. & Bernevig, B. A. Disconnected elementary band representations, fragile topology, and Wilson loops as topological indices: an example on the triangular lattice. *Phys. Rev. B* **99**, 045140 (2019).

49. Wieder, B. J. et al. Strong and fragile topological Dirac semimetals with higher-order Fermi arcs. *Nat. Commun.* **11**, 627 (2020).

50. Po, H. C., Watanabe, H. & Vishwanath, A. Fragile topology and Wannier obstructions. *Phys. Rev. Lett.* **121**, 126402 (2018).

51. Song, Z.-D., Elcoro, L., Xu, Y.-F., Regnault, N. & Bernevig, B. A. Fragile phases as affine monoids: classification and material examples. *Phys. Rev. X* **10**, 031001 (2020).

52. Song, Z.-D., Elcoro, L. & Bernevig, B. A. Twisted bulk-boundary correspondence of fragile topology. *Science* **367**, 794–797 (2020).

53. Peri, V. et al. Experimental characterization of fragile topology in an acoustic metamaterial. *Science* **367**, 797–800 (2020).

54. Kruthoff, J., de Boer, J., van Wezel, J., Kane, C. L. & Slager, R.-J. Topological classification of crystalline insulators through band structure combinatorics. *Phys. Rev. X* **7**, 041069 (2017).

55. Song, Z. & Fang, C. $(d-2)$-dimensional edge states of rotation symmetry protected topological states. *Phys. Rev. Lett.* **119**, 246402 (2017).

56. Soluyanov, A. A. & Vanderbilt, D. Wannier representation of $\mathbb{Z}_2$ topological insulators. *Phys. Rev. B* **83**, 035108 (2011).

57. Fang, C., Gilbert, M. J. & Bernevig, B. A. Bulk topological invariants in non-interacting point group symmetric insulators. *Phys. Rev. B* **86**, 115112 (2012).

58. Benalcazar, W. A., Bernevig, B. A. & Hughes, T. L. Quantized electric multipole insulators. *Science* **357**, 61–66 (2017).

59. Xiong, Z. et al. Corner states and topological transitions in two-dimensional higher-order topological sonic crystals with inversion symmetry. *Phys. Rev. B* **102**, 125144 (2020).

60. Wieder, B. J. & Bernevig, B. A. The axion insulator as a pump of fragile topology. Preprint at https://arxiv.org/abs/1810.02373 (2018).

61. Alexandradinata, A., Dai, X. & Bernevig, B. A. Wilson-loop characterization of inversion-symmetric topological insulators. *Phys. Rev. B* **89**, 155114 (2014).

62. Soluyanov, A. A. & Vanderbilt, D. Smooth gauge for topological insulators. *Phys. Rev. B* **85**, 115415 (2012).

63. Brandts, J. H. Matlab code for sorting real Schur forms. *Numer. Linear Algebra Appl.* **9**, 249–261 (2002).

## AUTHOR CONTRIBUTIONS
All authors contributed extensively to the work presented in this paper.

## COMPETING INTERESTS
The authors declare no competing interests.

## ADDITIONAL INFORMATION

**Supplementary information** is available for this paper at https://doi.org/10.1038/s41535-020-00300-7.

**Correspondence** and requests for materials should be addressed to C.O.

**Reprints and permission information** is available at http://www.nature.com/reprints

**Publisher's note** Springer Nature remains neutral with regard to jurisdictional claims in published maps and institutional affiliations.